Comparative Effects of Linearly and Circularly Polarized Illumination on Microwave-Induced Thermoacoustic Tomography

Yu He, Changjun Liu, *Senior Member, IEEE*, Li Lin, and Lihong V. Wang, *Fellow, IEEE*

***Abstract*—Homogeneous illumination is important in microwave-induced thermoacoustic tomography (TAT) because it directly determines the quantification of the reconstructed images of objects. In this work, we studied the effects of both linearly and circularly polarized microwave illuminations on TAT images. A customized horn antenna and a helical antenna working at 3 GHz were used to provide linearly polarized and circularly polarized illuminations, respectively. Based on our simulated and experimental results from tumor phantoms, the imaged patterns of the targets showed dependence on their permittivity. The target size and microwave wavelength within the target affected the microwave power distribution, which resulted in different reconstructed images. We analyzed the effect of the microwave penetration depth on TAT images as well. The images under circularly polarized illumination presented better quality than those under linearly polarized illumination. Hence, circularly polarized illumination can potentially better detect breast tumors in clinical applications.**

***Index Terms*—Imaging, microwave, polarization, thermoacoustic tomography (TAT).**

I. Introduction

MICROWAVE or RF-induced thermoacoustic tomography (TAT) has recently received considerable attention because of its great potential in biomedical applications, especially for detection of human breast tumors [1]–[6]. By combining the advantages of traditional microwave imaging and ultrasonic imaging, TAT simultaneously yields good resolution and contrast. Compared to laser-based photoacoustic imaging, TAT possesses greater penetration [7]. In TAT, short microwave pulses are applied to irradiate tissue. The tissue absorbs microwave energy and creates thermoacoustic waves by thermoelastic expansion. The generated acoustic waves carry information about the microwave absorption distribution of the tissue and are detected by an ultrasound transducer or a transducer array.

The primary contrast in TAT comes from differences in microwave energy absorption due to variations in dielectric properties. Malignant tissues, with higher dielectric loss than normal tissues, absorb more microwave energy and generate stronger acoustic waves [8]. The different absorption properties among different types of tissues permit the reconstruction of a distribution of microwave absorption. However, the thermoacoustic waves map primarily the boundaries among different tissues, and it is difficult to directly reconstruct the internal composition. Since the amplitude of the induced thermoacoustic signal is proportional to the absorbed microwave energy, which depends on both the absorption coefficient and the microwave illumination, the antenna should ideally illuminate the object homogenously. Otherwise, the image will reveal not only the variation in absorption coefficient, but also the inhomogeneous illumination, which will result in ambiguity in signal interpretation [9].

TAT most commonly uses horn antennas and helical antennas, which radiate microwaves in linear polarization and circular polarization, respectively [5], [10]. Under linearly polarized illumination, distortion was observed in TAT images [11]. The reconstructed images of a cylindrical object appeared to be split into two parts, a phenomenon that we have investigated previously [12]. However, the effects of circularly polarized illumination on TAT images have not been studied, and it is worth comparing the results from the two kinds of polarized illumination.

In this letter, we report the effects of antenna polarization, including both linear and circular polarization, on TAT images. Considering that the relation between the size of the object and the microwave wavelength λ_a within the object can influence the TAT images, we prepared two cylindrical tumor phantoms with different diameters. One was smaller than λ_a, and the other was greater than λ_a. A horn antenna and a helical antenna were used separately to illuminate the phantoms. Both the simulated and experimental results of linearly and circularly polarized illumination are presented. Moreover, the effects of the cylindrical phantoms' heights, which correspond to the penetration depth influence, were studied as well.

Manuscript received July 19, 2016; revised November 15, 2016; accepted January 7, 2017. Date of publication January 16, 2017; date of current version June 12, 2017. The work of Y. He was supported by the China Scholarship Council 201506240067 and the China 973 program 2013CB328902.

Y. He is with the Department of Biomedical Engineering, Washington University in St. Louis, St. Louis, MO 63130 USA, and also with the School of Electronics and Information Engineering, Sichuan University, Chengdu 610064, China (e-mail: yuhe@wustl.edu).

C. Liu is with the School of Electronics and Information Engineering, Sichuan University, Chengdu 610064, China (e-mail: cjliu@ieee.org).

L. Lin and L. V. Wang are with the Department of Biomedical Engineering, Washington University in St. Louis, St. Louis, MO 63130 USA (e-mail: lilin@wustl.edu; lhwang@wustl.edu).

Color versions of one or more of the figures in this letter are available online at http://ieeexplore.ieee.org.

Digital Object Identifier 10.1109/LAWP.2017.2652853

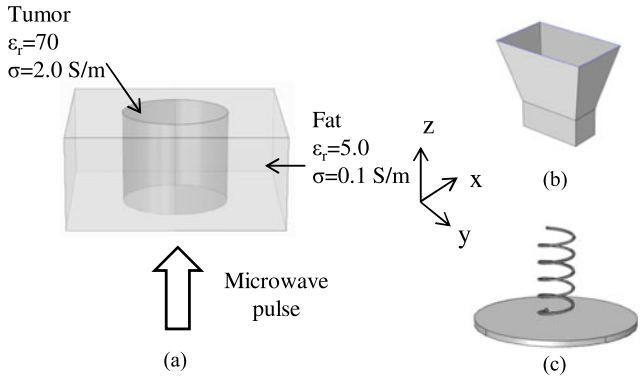

Fig. 1. (a) Simulation model. The phantom is made up of a tumor surrounded by fat. The microwave illumination is directed upward, along the z-direction. (b) Model of the horn antenna. (c) Model of the helical antenna.

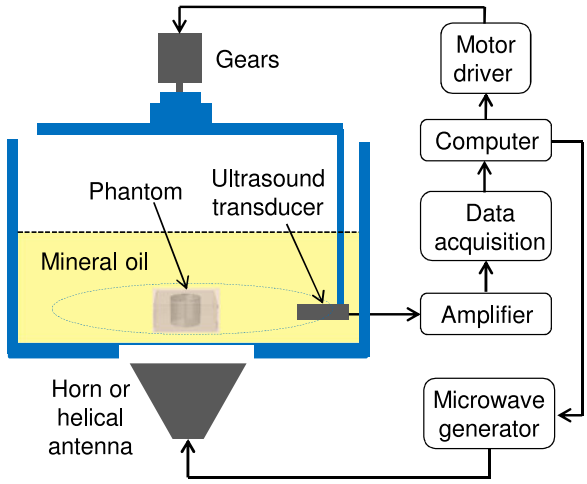

Fig. 2. Schematic of the experimental system.

II. Simulation Model and Experimental Setup

Microwave power absorption in biological tissues can be measured by the specific absorption rate (SAR), which is defined as the power absorbed per mass of tissue [13]

$$\mathrm{SAR}(\vec{r},t)=\frac{\sigma(\vec{r})\left|\vec{E}(\vec{r})\right|^2}{2\rho(\vec{r})}I(t) \tag{1}$$

where σ is the conductivity, $|E|$ is the amplitude of the electric field, ρ is the mass density, I is the microwave pulse function, t is time, and $\vec{r}$ represents the spatial location. The SAR is the microwave power density converted to heat.

A. Simulation Model

The tumor phantom used in the simulation was a dielectrically homogeneous cylinder with a relative permittivity of 70 and conductivity of 2.0 S/m, which is close to the dielectric properties of breast tumors [8]. The surrounding cube mimicked adipose tissue, and had a relative permittivity of 5.0 and conductivity of 0.1 S/m, as shown in Fig. 1(a). Considering that the wavelength λ_a of a 3-GHz microwave within the cylindrical tumor phantom is approximately 12 mm, we modeled two cylindrical tumor phantoms with diameters of 10 and 15 mm, respectively, and each 10 mm long.

Two differently polarized antennas working at 3 GHz were used to demonstrate the effect of antenna polarization on the SAR distribution in the tumor phantoms. For linear polarization, a pyramidal horn antenna [see Fig. 1(b)] was used, and for circular polarization, a helical antenna [see Fig. 1(c)] was used. The phantom was placed at the center of the aperture above the antenna. The antennas illuminated the phantom along the z-direction, and for the horn antenna the polarization was along the x-direction. Because the phantom was much smaller than the apertures of the antennas, the illuminating microwave in the apertures' vicinity could be regarded as a plane wave. We built the model in COMSOL multiphysics finite element modeling software to calculate the SAR distribution in the tumor phantom.

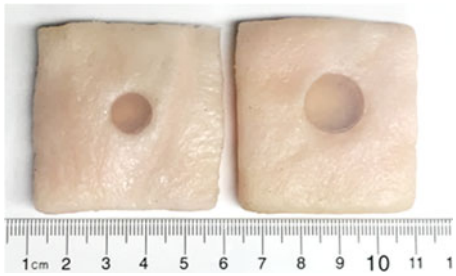

Fig. 3. Porcine fat phantoms in the experiment. Each phantom is with a small hole at the center filled with a cylindrical gel. The diameter of the gel on the left is 10 mm, and that on the right is 15 mm.

B. Experimental Setup

The setup developed for experimental validation is shown in Fig. 2. Microwave pulses transmitted from a 3-GHz microwave generator with a peak power of 60 kW were delivered to the sample through the antenna. The microwave pulse width was 0.6 μs, and the pulse repetition rate was 10 Hz. We used a custom-made horn antenna (WR284 horn antenna W/EEV flange, HNL Inc.) and a helical antenna (RA-4510-15 helix antenna, ROZENDAL Inc.), respectively, to illuminate the phantoms. The two antennas and phantoms used in the experiment had the same parameters as the models in the simulation. Each phantom had a hole in its center filled with water-based gel sample, as shown in Fig. 3. The gels, made of 3% agar and 97% water, mimicked breast tumors, and the porcine fat mimicked normal breast tissue. The phantoms were immersed in a plastic container filled with mineral oil, which is a good acoustic coupling liquid in TAT due to its low microwave and acoustic loss.

An ultrasonic transducer with a central frequency of 2.25 MHz and a diameter of 6 mm (V323, Panametrics-NDT) was used to receive the microwave-induced thermoacoustic signals. The transducer was fixed on a rotational apparatus and controlled by a step motor. It pointed horizontally to the rotation center and scanned around the phantom. The transducer and the connection cables were grounded with shielding mesh

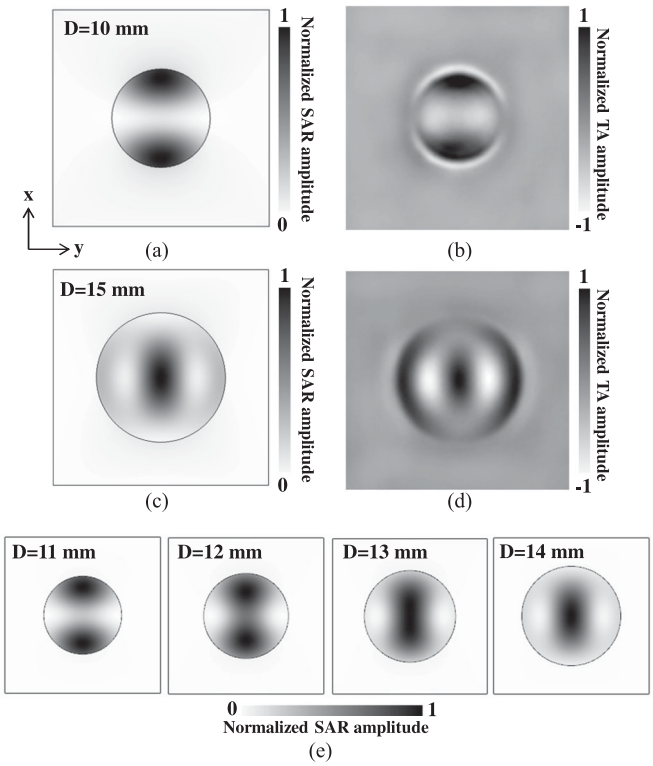

Fig. 4. Simulated and experimental results of the phantoms with different diameters under linearly polarized illumination. Simulated SAR distribution of the phantoms with diameters of (a) 10 and (c) 15 mm. Reconstructed images of the phantoms with diameters of (b) 10 and (d) 15 mm. (e) Simulated SAR distribution of phantoms with diameters ranging from 11 to 14 mm.

to reduce the microwave interference. The generated thermoacoustic signals received by the transducer were amplified by a 50-dB amplifier (5072 PR, Panametrics), then directed to a data-acquisition card with a sampling frequency of 20 MHz, averaged 50 times at each scanning stop for noise suppression, and finally transferred to a computer. The acquired thermoacoustic signals were used to reconstruct the distribution of the microwave absorption through our half-time back-projection algorithm [14].

III. Results and Discussions

The simulated SAR distribution and reconstructed images of the two tumor phantoms with different diameters under linearly polarized illumination are shown in Fig. 4. In the simulation, we averaged the SAR distribution of each cross section along the z-direction. In the measured results, we used the peak-to-peak value of the bipolar acoustic signal as the measure of thermoacoustic amplitude from the phantoms. The experimental results agreed well with the simulated results. When the diameter of the cylindrical tumor phantom was 10 mm, smaller than the relative wavelength λ_a, the distribution has a "bipolar" pattern with greater SAR values located near the boundaries intersecting with the antenna polarization direction, as shown in Fig. 4(a) and (b). When the diameter of the cylindrical tumor phantom was 15 mm, greater than the relative wavelength λ_a, the SAR distribution is completely changed, as shown in Fig. 4(c) and (d). A standing wave is formed in the phantom, and the antinodes can be observed at the center and at the edge, with the maximum values located at the center region. The 10-mm diameter phantom and 15-mm diameter phantom present two different distortions. We simulated the other four phantoms, with diameters ranging from 11 to 14 mm, to show the evolution of these changes, as shown in Fig. 4(e).

Here, the relative permittivity of the tumor phantom is 70, and the corresponding microwave wavelength within the phantom is 12 mm. If we change the relative permittivity of the tumor phantom to 30 in the simulation, the microwave wavelength within the phantom will be 18.3 mm, and the tumor phantom with a diameter of 15 mm will be smaller than the microwave wavelength. As a result, the SAR distribution in the tumor phantom is no longer the same as shown in Fig. 4(c). The "bipolar" pattern will occur in the phantom, just as in Fig. 4(a), which indicates that the SAR distribution depends on the object size and microwave wavelength within the object. We also note that the phantom will be more homogeneously illuminated when the diameter of the phantom is much smaller than the wavelength. However, the "bipolar" distortion always exists in the linearly polarized case.

Since the linear polarization of the microwave radiated by the horn antenna was along the x-direction, the electric field and the generated thermoacoustic signals were stronger at the boundaries of the sample along the x-direction. Therefore, the boundaries of the reconstructed image perpendicular to the x-axis are clear, while the boundaries parallel to the x-axis look ambiguous, as shown in Fig. 4(b). Unlike linear polarization, in which the electric field at a fixed point in space remains pointing at a fixed direction, the circular polarization involves the plane of polarization rotating in a corkscrew pattern, making one complete revolution over each wavelength. The circularly polarized wave radiates energy with the electric field in both the horizontal and vertical planes, as well as every plane in between. Theoretically, circularly polarized illumination provides more homogeneous illumination than linearly polarized illumination.

The results for the tumor phantoms under circularly polarized illumination are shown in Fig. 5. The SAR distribution in the phantoms is also related to their sizes. When the diameter of the cylindrical tumor phantom was smaller than the wavelength λ_a, the SAR distribution along the edge reaches its maximum and gradually decreases toward the center, as shown in Fig. 5(a) and (b). On the other hand, when the diameter of the cylindrical tumor phantom was greater than the wavelength λ_a, the SAR distribution is different, and is strongest at the center, as shown in Fig. 5(c) and (d). In a previous work [12], image distortion under linearly polarized illumination was alleviated by averaging two images obtained separately by two perpendicular illumination polarizations. However, under circularly polarized illumination, the "bipolar" pattern appearing in the linear polarization case no longer exists, and the boundaries of the reconstructed images are clearer for the whole circumference of the tumor phantom.

In the aforesaid analysis, the conductivity of the tumor phantoms is 2.0 S/m, and the corresponding $1/e$ penetration depth of the microwave amplitude at 3 GHz is close to the phantom height. If the height of the cylindrical tumor phantoms is smaller

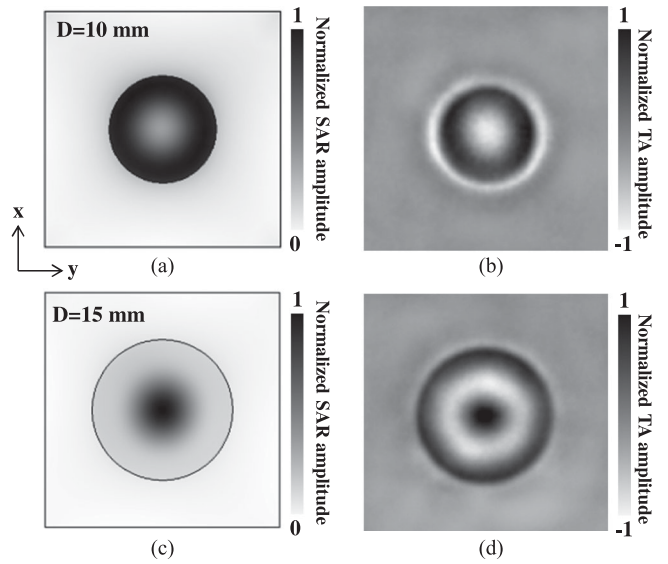

Fig. 5. Simulated and experimental results of the phantoms with different diameters under circularly polarized illumination. Simulated SAR distribution of the phantoms with diameters of (a) 10 and (c) 15 mm. Reconstructed images of the phantoms with diameters of (b) 10 and (d) 15 mm.

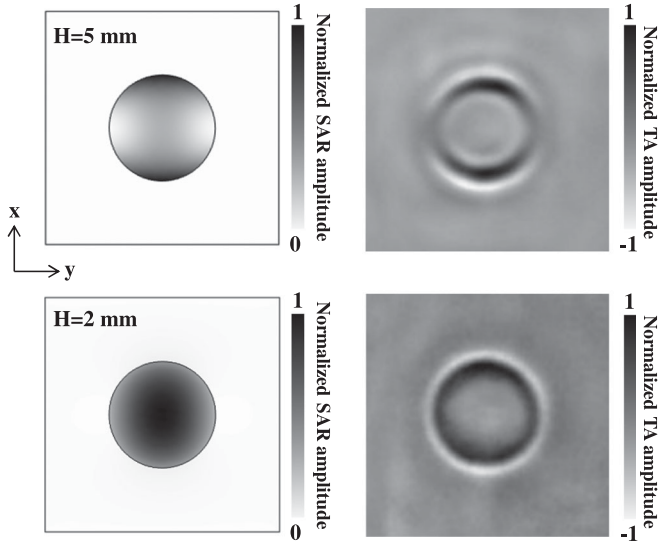

Fig. 6. Simulated and measured results of the phantoms with different heights under linearly polarized illumination. Simulated SAR distribution of the phantoms with heights of (a) 5 and (c) 2 mm. Reconstructed images of the phantoms with heights of (b) 5 and (d) 2 mm.

than the penetration depth, the images will be different. Here, we simulated and measured a 5-mm-tall cylindrical tumor phantom and a 2-mm-tall cylindrical tumor phantom, both with a diameter of 10 mm, under linearly polarized illumination, with the results shown in Fig. 6. For the 5-mm-high tumor phantom, the "bipolar" effect is much weaker than that in Fig. 3(a), as shown in Fig. 6(a) and (b). The 2-mm-high tumor phantom presents more homogeneous energy distribution, and the "bipolar" effect is not present, as shown in Fig. 6(c) and (d), demonstrating that the microwave penetration depth in the phantom also has great influence on the SAR distribution.

IV. Conclusion

In this letter, we compared the quality of the TAT images under linearly and circularly polarized illumination. Both simulations and experiments were carried out to demonstrate the image distortion mechanism in TAT. The dielectric properties of the target, the size of the target, and the polarization of the antenna all affect the TAT images. Specifically, for a cylindrical tumor phantom, the SAR distribution of the targets depends not only on the phantom size and microwave wavelength within the phantom, but also on the height of the phantom and penetration depth in the phantom. In addition, the circularly polarized illumination provides a more homogeneous illumination than the linearly polarized illumination, and it yields better images.

Although all the phantoms discussed here are homogeneous, and real tumors have more complicated shapes and nonuniform permittivity and conductivity, this study provides basic guidance for the preclinical and clinical applications of TAT.

References

[1] R. A. Kruger *et al.*, "Breast cancer in vivo: Contrast enhancement with thermoacoustic CT at 434 MHz—Feasibility study 1," *Radiology*, vol. 216, pp. 279–283, 2000.

[2] G. Ku *et al.*, "Thermoacoustic and photoacoustic tomography of thick biological tissues toward breast imaging," *Technol. Cancer Res. Treatment*, vol. 4, pp. 559–565, 2005.

[3] X. Wang, D. R. Bauer, R. Witte, and H. Xin, "Microwave-induced thermoacoustic imaging model for potential breast cancer detection," *IEEE Trans. Biomed. Eng.*, vol. 59, no. 10, pp. 2782–2791, Oct. 2012.

[4] L. V. Wang, X. Zhao, H. Sun, and G. Ku, "Microwave-induced acoustic imaging of biological tissues," *Rev. Sci. Instrum.*, vol. 70, pp. 3744–3748, 1999.

[5] R. A. Kruger *et al.*, "Thermoacoustic CT with radio waves: A medical imaging paradigm 1," *Radiology*, vol. 211, pp. 275–278, 1999.

[6] X. Wang, T. Qin, R. S. Witte, and H. Xin, "Computational feasibility study of contrast-enhanced thermoacoustic imaging for breast cancer detection using realistic numerical breast phantoms," *IEEE Trans. Microw. Theory Techn.*, vol. 63, no. 5, pp. 1489–1501, May 2015.

[7] M. Xu and L. V. Wang, "Photoacoustic imaging in biomedicine," *Rev. Sci. Instrum.*, vol. 77, p. 041101, 2006.

[8] M. Lazebnik *et al.*, "A large-scale study of the ultrawideband microwave dielectric properties of normal breast tissue obtained from reduction surgeries," *Phys. Med. Biol.*, vol. 52, pp. 2637–2656, 2007.

[9] M. Xu and L. V. Wang, "Pulsed-microwave-induced thermoacoustic tomography: Filtered backprojection in a circular measurement configuration," *Med. Phys.,* vol. 29, pp. 1661–1669, 2002.

[10] H. Ke, T. N. Erpelding, L. Jankovic, C. Liu, and L. V. Wang, "Performance characterization of an integrated ultrasound, photoacoustic, and thermoacoustic imaging system," *J. Biomed. Opt.*, vol. 17, pp. 0560101–0560106, 2012.

[11] M. Pramanik, G. Ku, C. Li, and L. V. Wang, "Design and evaluation of a novel breast cancer detection system combining both thermoacoustic (TA) and photoacoustic (PA) tomography," *Med. Phys.*, vol. 35, pp. 2218–2223, 2008.

[12] C. Li, M. Pramanik, G. Ku, and L. V. Wang, "Image distortion in thermoacoustic tomography caused by microwave diffraction," *Phys. Rev. E*, vol. 77, p. 031923, 2008.

[13] K. G. Zhu and M. Popović, "Spectral difference between microwave radar and microwave-induced thermoacoustic signals," *IEEE Antennas Wireless Propag. Lett.*, vol. 8, pp. 1259–1262, 2009.

[14] M. A. Anastasio *et al.*, "Half-time image reconstruction in thermoacoustic tomography," *IEEE Trans. Med. Imag.*, vol. 24, no. 2, pp. 199–210, Feb. 2005.